STScI | SPACE TELESCOPE SCIENCE INSTITUTE

Instrument Science Report ACS ISR 2018-02

Updates to Post-Flash Calibration for the Advanced Camera for Surveys Wide Field Channel

Nathan Miles

March 29, 2018

Abstract

This report presents a new technique for generating the post-flash calibration reference file for the Advanced Camera for Surveys (ACS) Wide Field Channel (WFC). The new method substantially reduces, if not, eliminates all together the presence of dark current artifacts arising from improper dark subtraction, while simultaneously preserving flat-field artifacts. The stability of the post-flash calibration reference file over time is measured using data taken yearly since 2012 and no statistically significant deviations are found. An analysis of all short-flashed darks taken every two days since January 2015 reveals a periodic modulation of the LED intensity on timescales of about one year. This effect is most readily explained by changes to the local temperature in the area surrounding the LED. However, a slight offset between the periods of the temperature and LED modulations lends to the possibility that the effect is a chance observation of the two sinusoids at an unfortunate point in their beat cycle.

1 Introduction

It has long been known that one of the many ways to alleviate the affects of charge transfer efficiency (CTE) losses on ACS/WFC is to increase the background of the exposure (Cox, 2006, Sokol et al., 2012). An increased background serves the purpose of filling the charge traps responsible for the reduction in CTE prior to the readout process, filling these

charge traps decreases their ability to trap additional electrons during the readout process thus improving the overall CTE. One simple way to increase the background level is through post-flash illumination via the LED lamp mounted between the CCD and the filter wheels (Ogaz et al., 2014).

The ACS team began post-flashing the calibration darks (Ogaz et al., 2015) in January of 2015 to mitigate the CTE effects. The capability for post-flash subtraction has been supported since `CALACS` version 8.1.3. Complementary post-flash calibration reference files have been generated yearly for use in the `FLASHCORR` step of `CALACS` (Lucas, 2016). In the following sections we describe a pilot program designed to improve the quality of the post-flash reference file, the steps taken to create the newest post-flash reference file, an analysis of the newest post-flash reference file, and finally, a study of the ACS post-flash reference files over time.

2 Pilot Program

2.1 Motivation

The post-flash reference file suffers from two main types of artifacts, dark current and flat-field, which are highlighted in Figure 1. The flat-field artifacts are caused by the presence of dust specks along the optical path between the LED and the CCD, whereas the dark current artifacts are a direct result of an improper dark subtraction. The improper dark subtraction manifests in either an over or under subtraction of the true dark current present in the raw post-flash images.

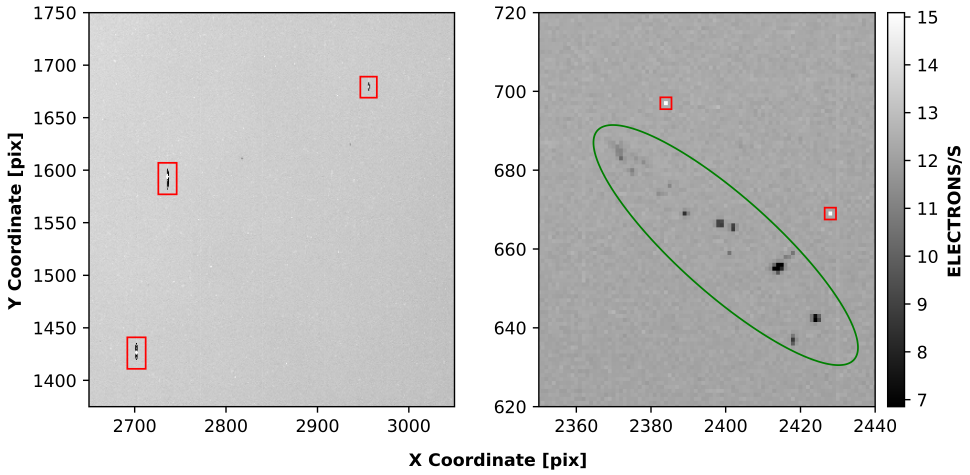

Figure 1: An example of the two types of artifacts in the post-flash reference file for 2016, 2141719ij_fls.fits. The dark current artifacts are outlined in red and the flat-field artifacts are outlined in green.

Over subtraction results in the present of dark spots in the final calibrated image, while the under subtraction results in the presence of hot pixels. The majority of the dark current artifacts are transient and change position year-to-year, whereas all of the flat-field artifacts appear in the same exact position in every post-flash image.

Since the dark current artifacts arise from an improper dark subtraction, a pilot program (15392, PI Miles) was approved to take short and long flash exposures such that the total

sum of the EXPTIME (t_E) and FLASHDUR (t_F) header keywords was held constant. By holding the total sum constant, the LED signal may be isolated as follows. Let $p(x, y)$ represent an arbitrary pixel located at (x, y) on the CCD, then its value, in electrons, can be expressed as a linear combination of the various contributions from each of the different sources. For a bias-corrected, post-flashed dark frame, the sources are the dark current ($dc(x, y)$) in electrons/sec, and LED signal ($fr(x, y)$) in electrons/sec, so we have:

$$p(x, y) = t_d * dc(x, y) + t_F * fr(x, y) \tag{1}$$

The total time for dark current to accumulate (t_d) is the sum of the commanded exposure time (t_E), the flash duration (t_F), and the commanding overheads (δt). Since the commanding overheads are consistent from image to image, if pairs of images are taken with the constraint that $t_{F1} + t_{E1} = t_{F2} + t_{E2}$, then we will have $t_{d1} = t_{d2}$. Thus, by differencing the long (p_1) and short (p_2) pairs of flash exposures, we can isolate the LED signal as follows:

$$\begin{aligned} p_{final}(x, y) =& p_1(x, y) - p_2(x, y) \\ =& [t_{d1} * dc(x, y) + t_{F1} * fr(x, y)] \\ & - [t_{d2} * dc(x, y) + t_{F2} * fr(x, y)] \\ =& (t_{F1} - t_{F2}) * fr(x, y) \\ fr(x, y) =& \frac{p_{final}(x, y)}{t_{F1} - t_{F2}} \end{aligned} \tag{2}$$

2.2 Observations

To implement the concepts described in the previous section, a total of 6 internal HST orbits were used to take short and long-flash pairs (Table 1). For both short and long exposure images the post-flash current level was LOW and the shutter position was set to Shutter B in accordance with the parameters established in ACS ISR 2014-01 (Ogaz et al., 2014).

IPPPSOOT	FLASHDUR(s)	EXPTIME (s)
jdq501fuq_raw.fits	341.0	0.5079
jdq502evq_raw.fits	341.0	0.5079
jdq503f5q_raw.fits	341.0	0.5079
jdq504f9q_raw.fits	341.0	0.5079
jdq505flq_raw.fits	341.0	0.5079
jdq506fqq_raw.fits	341.0	0.5079
jdq501fvq_raw.fits	4.5	337.0
jdq502ewq_raw.fits	4.5	337.0
jdq503f6q_raw.fits	4.5	337.0
jdq504faq_raw.fits	4.5	337.0
jdq505fmq_raw.fits	4.5	337.0
jdq506frq_raw.fits	4.5	337.0

Table 1: Observations from Proposal 15392

3 Reference File Creation

The RAW data products were downloaded from MAST and processed via CALACS (Lucas, 2016) with only DQICORR, BIASCORR, and BLEVCORR set to PERFORM. The short and long exposure frames were then separated and combined using ACSREJ to produce cosmic ray cleaned short and long-flash images. The SCI extensions of the final post-flash file were calculated according to Equation 2. The ERR extensions were calculated according to Equation 3, where σ_{long} and σ_{short} are the ERR extensions of the stacked long- and short-flash images.

$$\sigma = \sqrt{\sigma_{long}^2 + \sigma_{short}^2} \tag{3}$$

3.1 Visual Inspection

After creating the new post-flash reference file, the first step was to examine the same regions of the post-flash file presented in Figure 1. On the left side of Figure 2, the scars from over subtraction have been substantially reduced in size and are now small enough to be smoothed out. On the right side, the hot pixels that were once present above the flat-field artifacts have completely disappeared while the flat-field artifact remains.

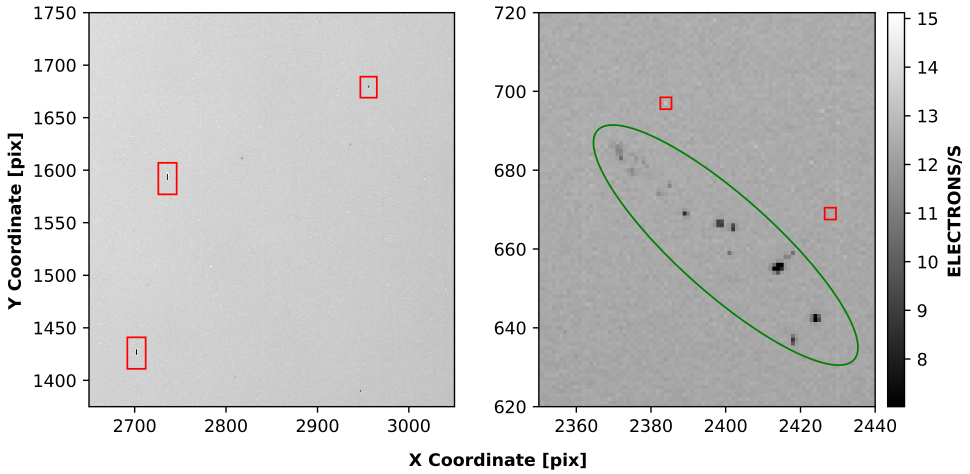

Figure 2: Same as Figure 1 but for the post-flash file created as described in the Reference File Creation section. The presence of the dark current artifacts are substantially reduced using the new method.

3.2 Smoothing

To remove any minor imperfections remaining after the differencing, a local median smoothing routine was applied. For each pixel, a box, 30 by 30 pixels in size, was drawn in which the median and standard deviation were calculated. If the pixel value, $p(x, y)$, satisfies Equation 4 then it is replaced with the median value of the box, otherwise it is left alone and the next pixel is analyzed.

$$|p(x, y) - median_{box}| \geq 5 * \sigma_{box} \tag{4}$$

A catalog of flat-field artifacts are masked out during smoothing procedure. The final result of the smoothing can be seen in Figure 3. Note the unchanged presence of the flat-field artifact on the right and the removal of residual dark current imperfections on the left.

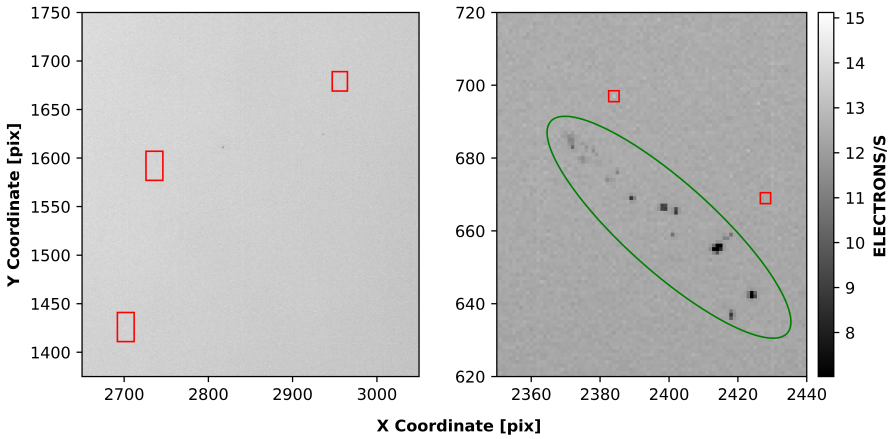

Figure 3: The final result of the local median smoothing demonstrating that the dark current artifacts have been removed, while the flat-field artifacts remain.

The final post-flash reference file (Figure 4) was delivered to the HST Calibration Reference Data System[1](CRDS) on January 4, 2018 and is available for use with data taken after May 5th, 2017. The horizontal and vertical lines segment the image into four quadrants that have been marked by their readout amplifiers (A, B, C, or D).

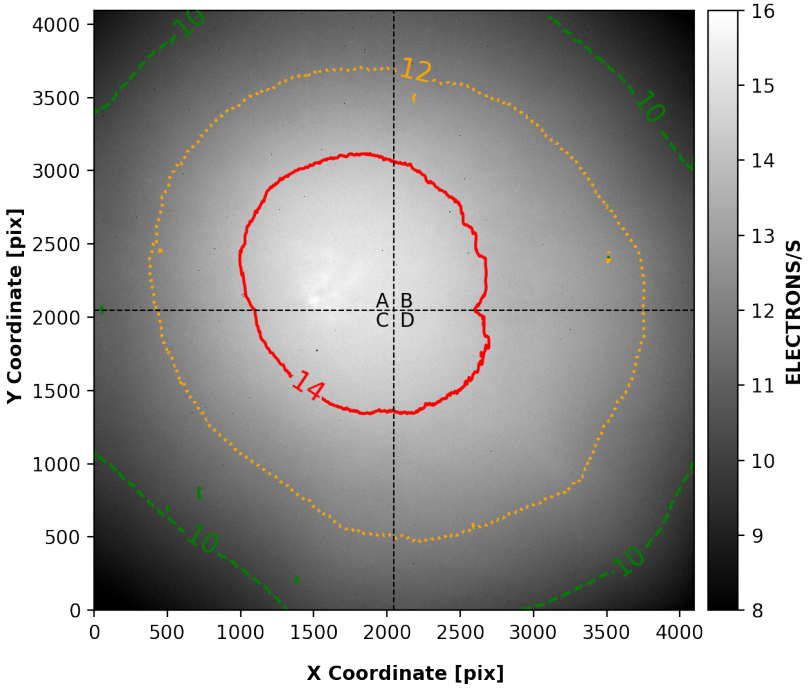

Figure 4: The post-flash reference file created by applying the new method to the data from Proposal 15392. Contours at 10, 12, and 14 electrons per second have been overlaid to accentuate the non-uniformity of the LED illumination pattern.

[1]https://hst-crds.stsci.edu

4 Analysis

4.1 Non-Uniform Illumination

The non-uniform illumination pattern of ACS/WFC LED was found to have variations of 50% across the field of view (Ogaz et al., 2014). To probe the affect differencing has on the illumination pattern, the CCD was divided up into 16 equal partitions, each one 1024 by 1024 pixels in size (Figure 5).

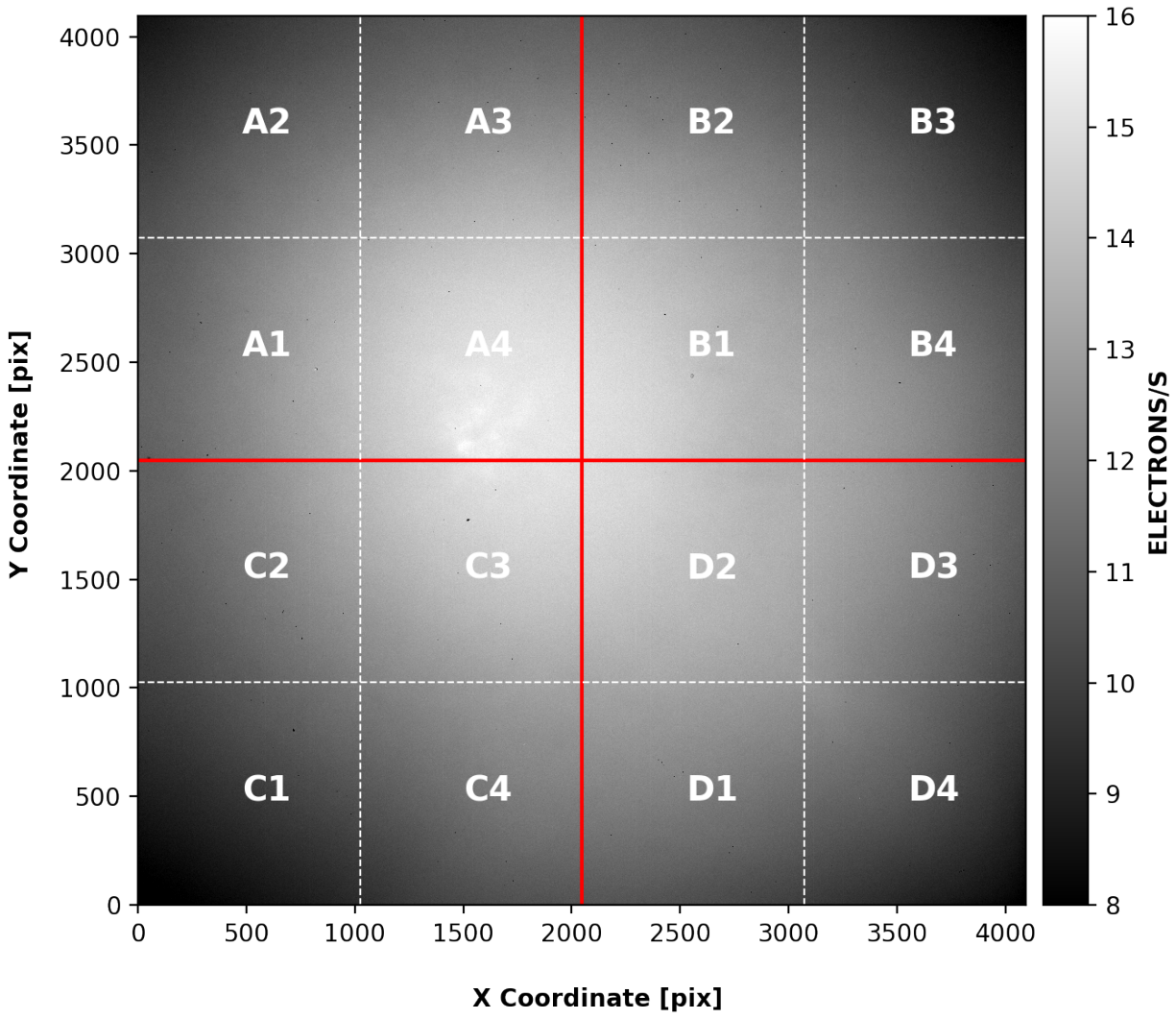

Figure 5: The 16 partitions labeled according to the readout amplifier used to readout each of the 4 larger quadrants sectioned off by the solid red lines. The chip gap between WFC1, top two quadrants, and WFC2, bottom two quadrants, has been omitted for clarity.

For each partition, the mean of the SCI and ERR extensions, the standard deviation of the SCI extension, and fraction of the total signal were calculated. If the illumination were uniform, then each of the 16 partitions would contain exactly $\frac{1}{16} = 0.0625 = 6.25\%$ of the total flux, but a quick glance of the last column in Table 2 reveals a distribution of values with a mean of 6.25% and $\sigma = 0.73\%$. Next, comparing the maximum (A4) and minimum (C1) mean values of the partitions reveals a maximum variation of ∼51% across the field view.

Partition	$\overline{p}_{SCI}$ [e pix^{-1} s^{-1}]	$\overline{p}_{ERR}$ [e pix^{-1} s^{-1}]	σ_{SCI} [e pix^{-1} s^{-1}]	%
A1	12.256	0.079	0.918	6.363
A2	10.673	0.074	0.936	5.541
A3	12.230	0.079	0.961	6.349
A4	14.685	0.087	0.523	7.623
B1	13.958	0.084	0.628	7.246
B2	11.903	0.078	0.910	6.180
B3	10.066	0.072	0.963	5.226
B4	11.961	0.078	0.845	6.210
C1	9.705	0.071	0.906	5.038
C2	11.714	0.077	0.880	6.081
C3	13.927	0.084	0.766	7.230
C4	11.484	0.077	0.845	5.962
D1	11.801	0.078	0.799	6.127
D2	13.839	0.084	0.513	7.184
D3	12.024	0.079	0.819	6.242
D4	10.397	0.073	0.985	5.397

Table 2: Statistics calculated for each of the 16 partitions. For each partition, $\overline{p}_{SCI}$ is the mean of the SCI extension, $\overline{p}_{ERR}$ is the mean of the ERR extension, σ_{SCI} is the standard deviation of the values in the SCI extension, and % is the percentage of total flux measured in each partition.

4.2 Post-Flash Reference File Over Time

The ACS Team has been generating a yearly post-flash reference file since 2012. A statistical comparison of all post-flash reference files wis performed to check for losses in the optical power output of the LED. To accomplish this, 27 boxes, 100 by 50 pixels in size, are placed across the field of view of WFC1 and WFC2. The locations were judiciously chosen to sample the non-uniformity of the LEDs illumination pattern on WFC2 and then reflected about the chip gap to produce corresponding locations on WFC1 (Figure 6b and Figure 6a). The effects of radiation on the LED were characterized by the manufacturer, OptoDiode, and it was found that the optical power output of the LED did not degrade until the total radiation dosage from neutrons was above $\sim 6\text{x}10^{11}\frac{n}{cm^2}$ (OptoDiode, 2017). A second independent test (Johnston, 2000) found similar results demonstrating that the optical power output did not degrade until the total radiation dosage from protons was well above $\sim 1\text{x}10^{11}\frac{p}{cm^2}$.

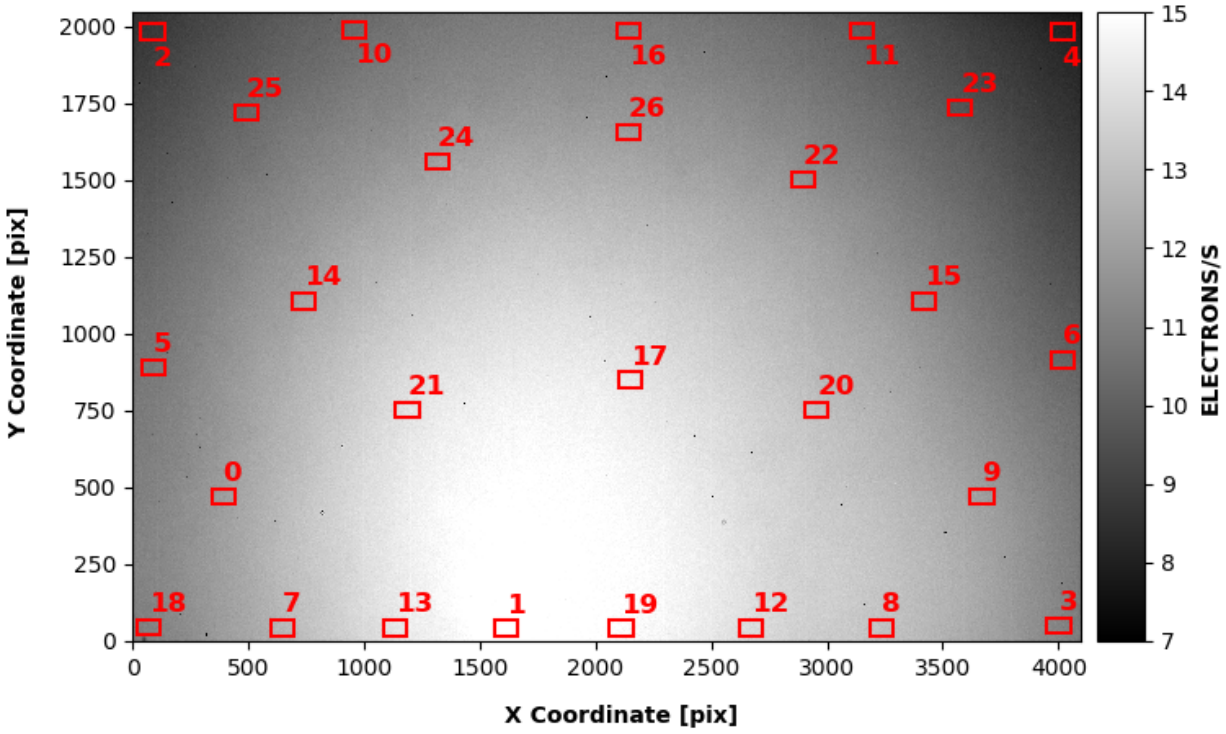

(a) Locations of the 27 boxes for WFC1

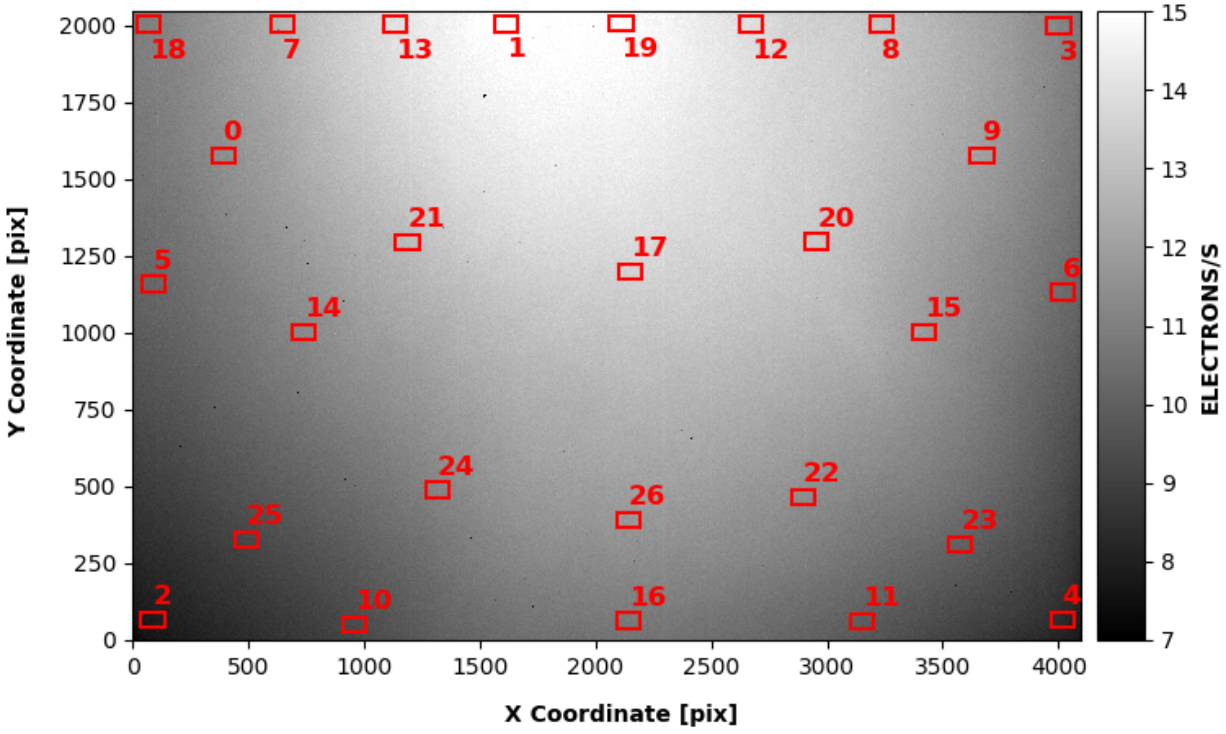

(b) Locations of the 27 boxes for WFC2

Figure 6

The ACS instrument has been in the harsh radiation environment of space for almost 16 years. An analysis of every single ACS/WFC dark ever taken reveals an average cosmic ray flux on the order of $\sim 1.2\frac{events}{s*cm^2}$ (Miles et al., ISR in prep.), where one event is defined to be one cosmic ray detection. A short description of the process used to identify and characterize cosmic rays is detailed in Appendix A. The composition of cosmic rays is roughly 90% H^+ (i.e. protons) and so the total radiation dosage of the instrument is roughly $\sim 6x10^8\frac{p}{cm^2}$. The LED and the ACS/WFC CCD's receive approximately the same radiation dosage from cosmic rays. This implies that there should be no statistical deviations in the optical power output over time. To test this, the mean of both the SCI and ERR extension for all 27 boxes labeled in Figure 6 were analyzed as a function of time.

For both chips, there are no statistically significant deviations observed in the post-flash reference files over the 6 year period from early 2012 to late 2017 at any location across the field of view. A random sample of boxes from across the field of view were chosen to graphically demonstrate the results for each chip. Figures 7a and 7b, show the full range of all 8 boxes from the lowest level of ~8 electrons/s to the highest level of ~15 electrons/s. Figures 8a and 8b, demonstrate the consistency of all the measurements to within their uncertainties.

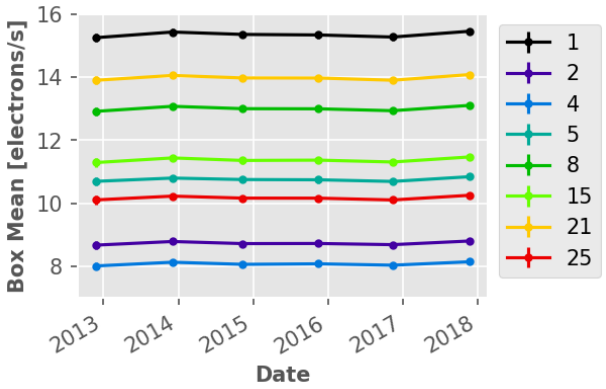

(a) Mean of arbitrary boxes for WFC1. At this scale data points are larger than error bars.

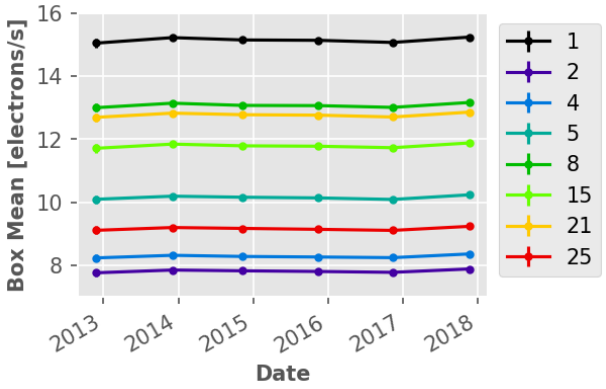

(b) Mean of arbitrary boxes for WFC2. At this scale data points are larger than error bars.

Figure 7

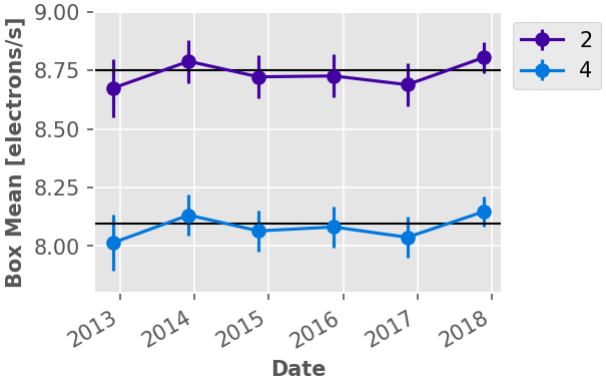

(a) Same as Figure 7a, but zoomed in on boxes 2 and 4 from WFC1.

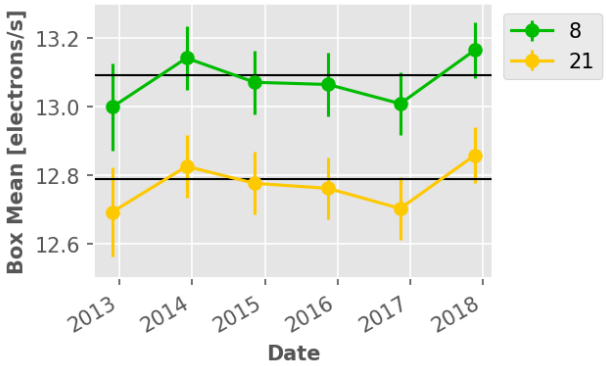

(b) Same as Figure 7b, but zoomed in on boxes 8 and 21 from WFC2.

Figure 8

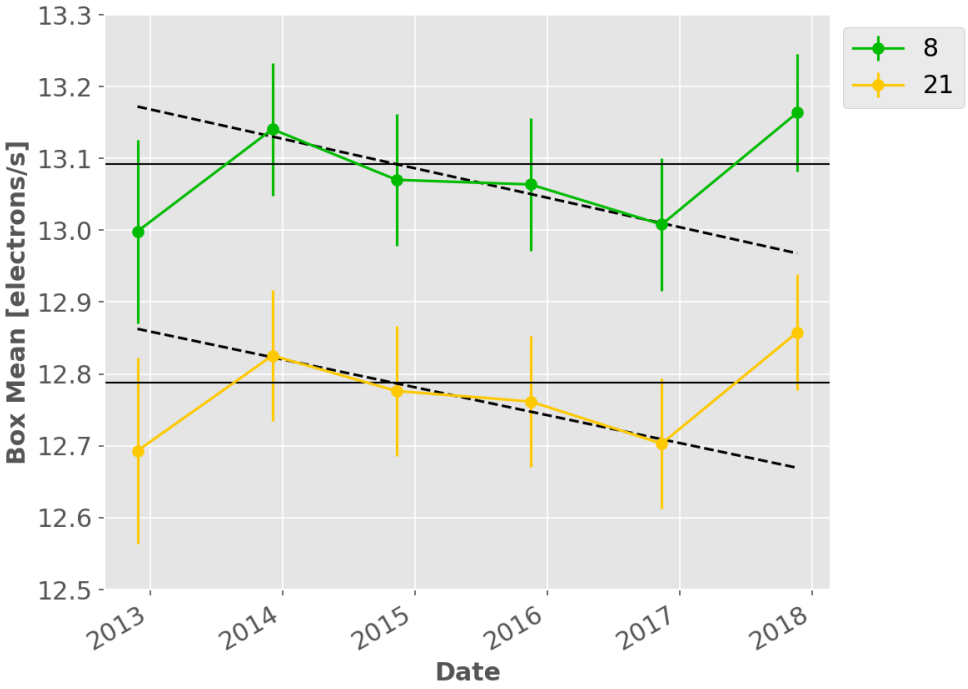

Figure 9: Mean of boxes 8 and 21 on WFC2 fit with separate linear functions from late 2013 to late 2016. The line of best fit for box 8, top dashed line, has a slope of -0.0415 e^-/s/pix/yr and the line of best fit for box 21, bottom dashed line, has a slope of -0.0397 e^-/s/pix/yr. The horizontal, solid black lines are the means of each distribution of values for the two boxes plus an empirical offset of 0.018 e^-/s.

Even though the measurements are all consistent, there is an apparent trend in decreasing intensity observed from 2014 to late 2017 (Figure 9). To investigate this trend, a similar analysis is performed using every single flashed-short dark taken as part of the yearly ACS CCD Daily Monitor calibration program from 2015 to present[2]. As part of the calibration program, two flashed-short darks are taken at intervals of 3 times per week with an exposure time of 0.5 seconds and a flash duration of 4.6 seconds. Since 2015, a total of 944 flashed-short darks have been taken and all 944 raw images were processed with CALACS to generate bias-corrected FLTs with 0.5 seconds of dark current and 4.6 seconds of flash. To mitigate the effects of cosmic rays, the median of each box was examined as a function of time.

Over the ∼3 year period, there is no observable decline in the optical power output of the LED, although there is interesting periodicity. For box 2, ∼64% of the data points fall within 1% of the median of the distribution of box 2 values and 93% fall within 2% (Figure 10). For box 19, ∼70% of the data points fall within 1% of the median of the distribution of box 19 values and 95% fall within 2% (Figure 11). From Figures 10 and 11, the periodicity of the optical power output appears to be in phase with aphelion and perihelion of Earth's orbit.

[2]Proposal ID: 14395, 14396, 14397, 14506, 14517, 14518, 14946

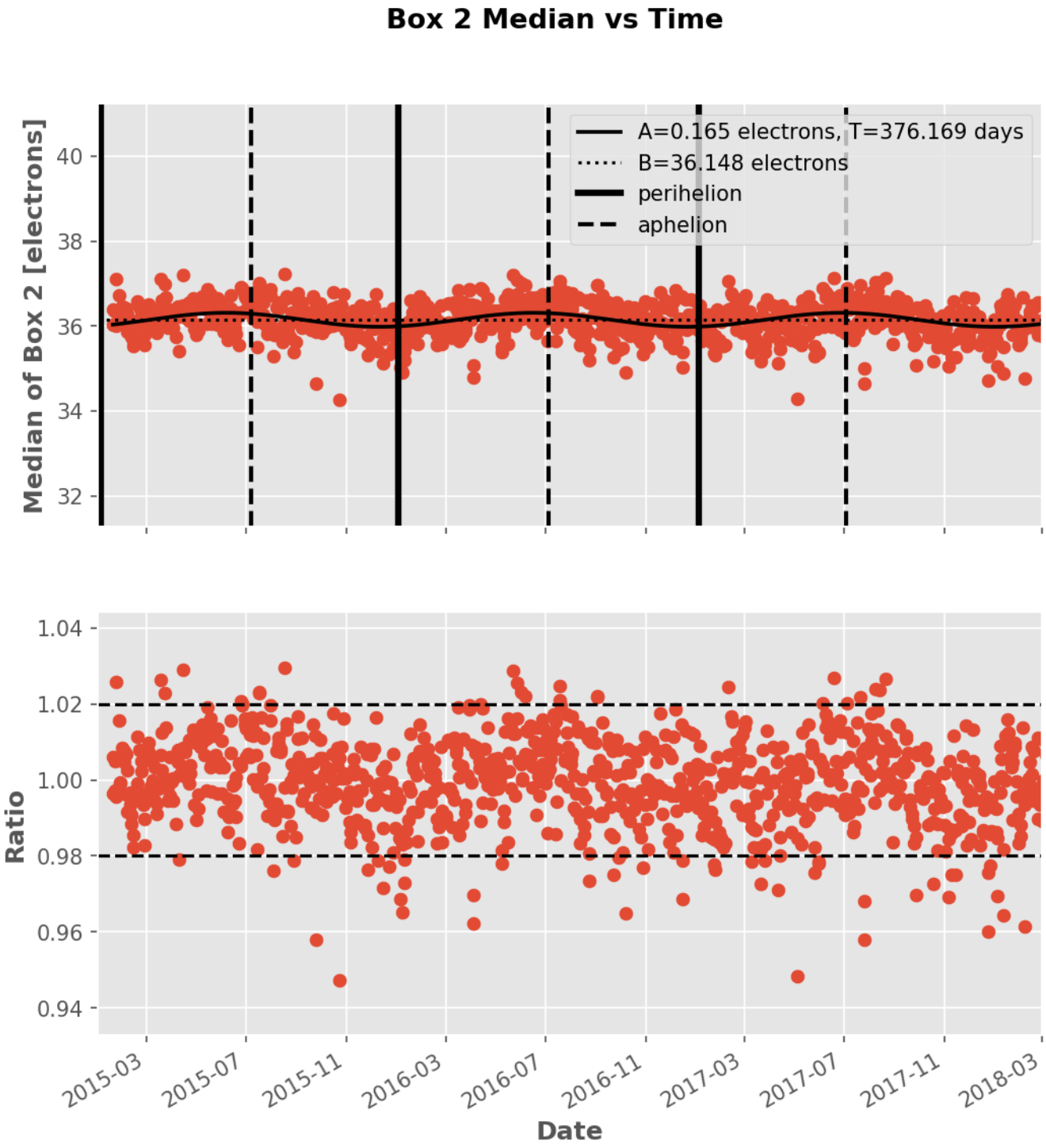

Figure 10: The top plot shows the variation of the median value of Box 2 as a function of time using all of the flashed-short darks. The bottom plot is a median normalized version of the top plot showing that the variations are about 4% peak-to-peak.

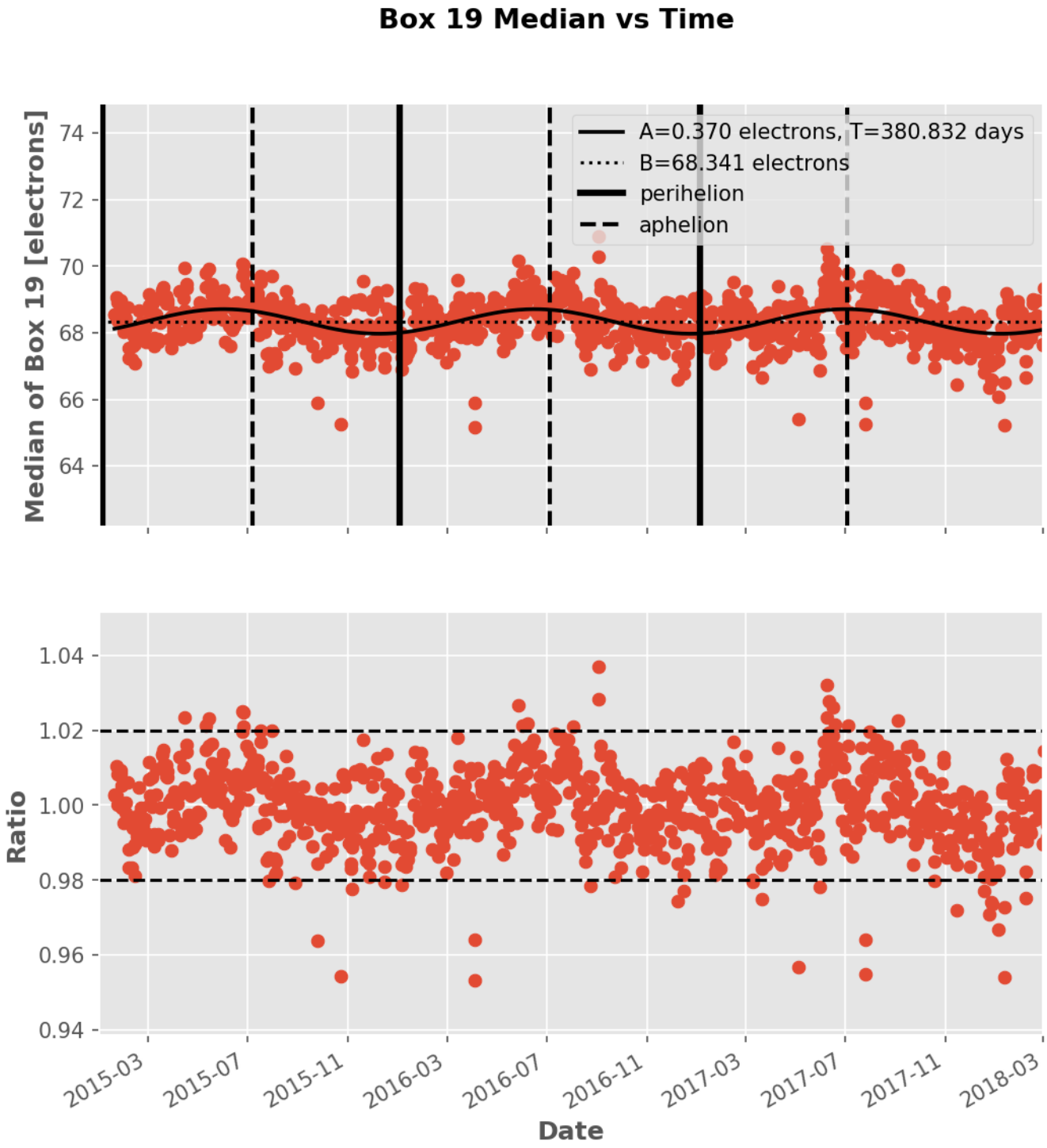

Figure 11: The top plot shows the variation of the median value of Box 19 as a function of time using all of the flashed-short darks. The bottom plot is a median normalized version of the top plot showing that the variations are about 4% peak-to-peak.

To quantify the periodic behavior, the median for all 27 of the boxes was analyzed as a function of time and fit with the function described by Equation 5. The parameters of interest are the amplitude, A, the period, T, and the offset, B, the values and uncertainties from each fit are reported in Tables 3 and 4 for WFC1 and WFC2, respectively.

$$f(t) = A * sin(\frac{2\pi}{T}t - \phi) + B \tag{5}$$

The ratio of the amplitude, A, and the offset, B, for each fit gives the magnitude of the effect. The ratio is roughly constant across the field of view with an average value of 0.49% and a $\sigma = 0.05\%$ indicating that the level of modulation is independent of the signal strength. The average of all the periods is $< T >= 376.52$ days and error in that value is $\sigma_{<T>} = 8.31$ days, implying that the average period extracted from the LED signal is within 1.35 $\sigma_{<T>}$ of the earth's orbital period.

Box Number	A [electrons]	σ_A [electrons]	B [electrons]	σ_B [electrons]	T [days]	σ_T [days]
0	0.246731	0.000580	52.593747	0.000297	388.643924	53.150769
1	0.354308	0.001179	69.827227	0.000606	381.961317	49.351470
2	0.174350	0.000353	36.141369	0.000181	380.053440	59.382028
3	0.249445	0.000595	51.146620	0.000307	377.809381	48.279803
4	0.235630	0.000382	38.161134	0.000196	383.550263	36.518666
5	0.231390	0.000490	46.951748	0.000251	380.784799	47.031304
6	0.253352	0.000492	47.642926	0.000253	378.384306	38.545742
7	0.272642	0.000713	58.061579	0.000367	380.342037	49.454801
8	0.316003	0.000769	60.103862	0.000396	379.845452	39.777687
9	0.279120	0.000616	54.862482	0.000317	381.215898	41.159025
10	0.161202	0.000430	42.842635	0.000224	373.495196	83.183525
11	0.282462	0.000561	45.282663	0.000286	384.802927	36.931100
12	0.353018	0.000852	63.824799	0.000437	380.062026	34.692048
13	0.313157	0.000945	64.433879	0.000488	378.080582	49.108518
14	0.221676	0.000573	51.825242	0.000293	382.053984	60.115082
15	0.274148	0.000632	54.287476	0.000327	376.407033	42.417231
16	0.313028	0.000589	49.532879	0.000300	384.708829	31.467623
17	0.350701	0.000826	62.390337	0.000424	380.274099	34.173432
18	0.274346	0.000549	50.534017	0.000282	381.127338	38.224255
19	0.384490	0.000951	68.330656	0.000486	383.420548	33.515976
20	0.319290	0.000735	60.638641	0.000382	374.515212	35.877953
21	0.242632	0.000732	59.027651	0.000376	380.903604	64.048271
22	0.315841	0.000610	52.357547	0.000316	376.569669	31.326622
23	0.250549	0.000531	46.139295	0.000271	385.410249	44.658276
24	0.235945	0.000575	51.076710	0.000292	387.587170	54.720664
25	0.186263	0.000419	42.311649	0.000216	378.445468	61.132450
26	0.313850	0.000655	53.863007	0.000339	376.742452	34.156298

Table 3: WFC1 results from fitting each box as a function of time with the sinusoid in Equation 5.

Box Number	A [electrons]	σ_A [electrons]	B [electrons]	σ_B [electrons]	T [days]	σ_T [days]
0	0.229882	0.000557	52.604239	0.000289	385.160214	59.381487
1	0.337777	0.001143	69.837639	0.000594	379.536347	52.884619
2	0.166590	0.000339	36.146082	0.000177	378.028489	63.346382
3	0.245141	0.000572	51.149471	0.000299	376.726622	48.871099
4	0.227489	0.000363	38.166158	0.000189	381.929509	37.870082
5	0.223070	0.000467	46.956577	0.000244	379.536173	49.351780
6	0.235761	0.000476	47.653590	0.000249	375.239496	43.511193
7	0.259933	0.000686	58.069556	0.000357	377.852717	52.674394
8	0.311774	0.000741	60.106421	0.000386	379.252037	40.065502
9	0.263513	0.000595	54.872056	0.000310	378.681900	44.846941
10	0.155554	0.000420	42.846712	0.000218	370.841795	83.787473
11	0.267563	0.000538	45.291409	0.000280	382.805203	40.545868
12	0.340065	0.000828	63.832494	0.000432	378.579918	37.230245
13	0.305391	0.000915	64.438968	0.000477	376.546969	50.310916
14	0.210982	0.000555	51.831753	0.000289	379.786954	65.567029
15	0.262932	0.000615	54.294557	0.000321	374.272613	44.792253
16	0.296862	0.000566	49.542363	0.000294	382.794121	34.604935
17	0.330420	0.000793	62.402706	0.000414	377.571213	37.548472
18	0.254467	0.000534	50.547214	0.000277	376.488718	42.237738
19	0.373197	0.000921	68.337460	0.000479	382.174468	35.469020
20	0.303366	0.000711	60.648729	0.000373	371.913627	38.348595
21	0.237210	0.000705	59.030986	0.000367	379.806822	65.950555
22	0.302780	0.000592	52.366715	0.000307	373.664761	32.108675
23	0.241056	0.000509	46.144753	0.000265	384.192079	47.836847
24	0.222411	0.000553	51.084149	0.000287	386.356541	61.693520
25	0.184399	0.000402	42.312982	0.000210	377.564735	61.099337
26	0.295591	0.000640	53.876081	0.000332	372.165143	35.734291

Table 4: WFC2 results from fitting each box as a function of time with the sinusoid in Equation 5.

For ACS/WFC, the LED is situated directly on top of the CCD housing which is in thermal contact with the aft-shroud via the heat pipe system allowing heat transfer from the ACS thermoelectric coolers to the radiators. The best measurement of the CCD housing temperature where the LED is situated is the JWXWINDT probe, which samples the temperature near the window of the housing every two seconds (Figure 12). An analysis of the JWXWINDT readings from 2010 through 2017 reveals a similar periodicity with the maximum temperatures occurring at perihelion and the minimum temperatures occurring at aphelion. Figure 13 shows a subset of the JWXWINDT data covering the same time period as the flashed-short darks with the best fit sinusoid overlaid (solid black line). The period derived from the ∼8 years of temperature data is 362.57 ± 0.06 days.

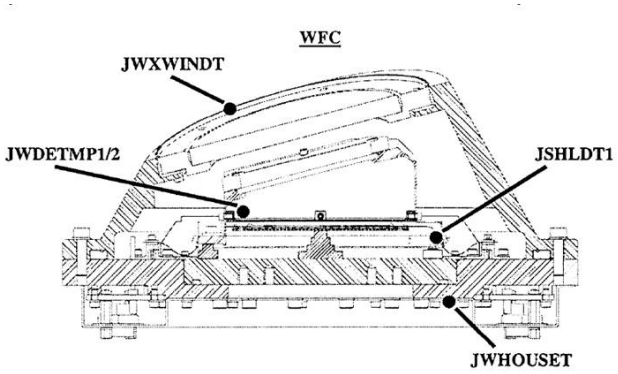

Figure 12: Schematic of the ACS/WFC CCD Housing with the locations of the four temperatures used to monitor ACS/WFC.

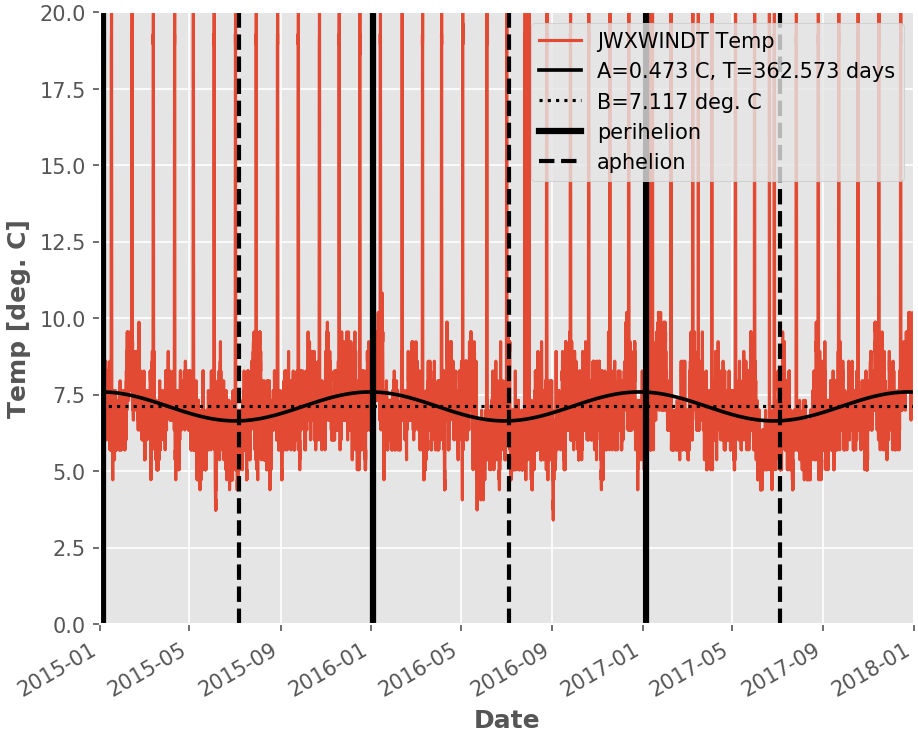

Figure 13: The JWXWINDT temperature readings as a function of time. A rolling average has been applied to the raw data to compute hourly values from the 2 second samples. The solid line is the best-fit sinusoid described by Equation 5 derived using the raw data. The large vertical spikes reaching up to 20°C are the 6 hour anneals.

The optical power output of the OD800W LED is negatively correlated with its ambient temperature (OptoDiode, 2017). Therefore, we postulate that the cause of the modulation of the LEDs signal is a change in local temperature of the CCD housing arising from changes in the incident solar flux as the Earth progresses through its orbit. Looking at Figure 14 we see that the two signals are approximately π radians out of phase and because the phase shift is not exactly π, there is a beat frequency for these two signals. The beat frequency is $f_{beat} = f_{temp} - f_{led} = 1/362.57 - 1/376.52 = 0.000102$ cycles/day, assuming the two signals are unrelated implies it would take roughly 9786 days, or 26 years, for these two signals to complete one full cycle. Unfortunately, the observation period where we have overlapping data is only 3 years long and so it is not possible for us to rule out the possibility that we could be observing the period of the cycle where the two signals are approaching a phase shift of π radians, by chance. The only way to rule this out is to collect more data and see if either the phase drifting continues or the quality of the fit improves and the $\sim$14 day discrepancies between the two periods decreases.

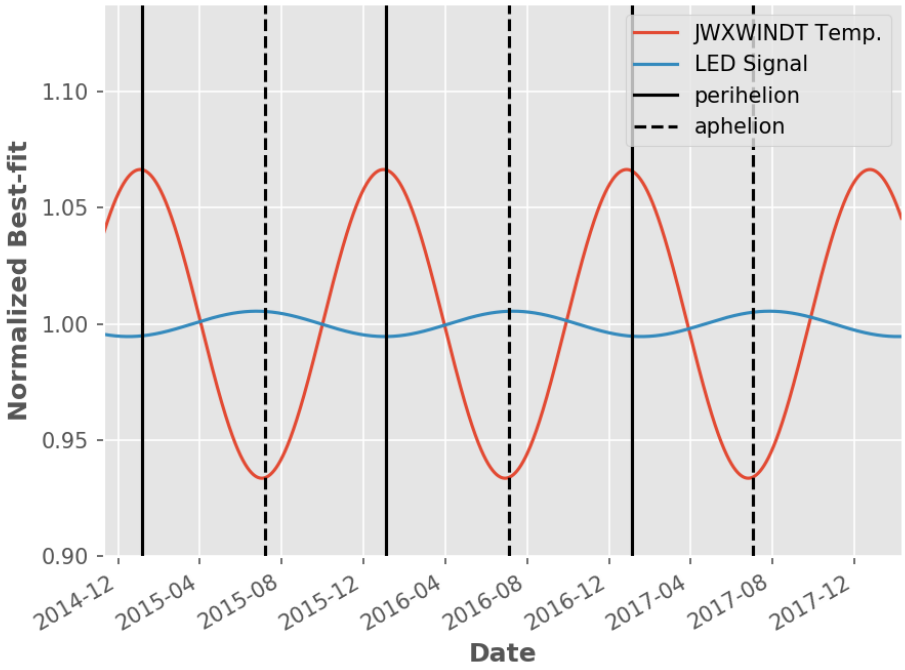

Figure 14: A comparison of the best-fit sinusoids for the LED and JWXWINDT datasets.

5 Recommendations to Users

The current scenarios in which post-flashing is most useful are observations with low background (< 20 electrons) and/or observations of relativity faint sources. For observations with low background, we recommend that users avoid post-flashing and instead lengthen the

total exposure time until the background is close to or higher than the threshold of ∼20 electrons (Sokol et al., 2012). For faint sources that subtend less than 5 arcsec, we also recommend that users avoid post-flashing and instead use the WFC1-CTE aperture to place the source within 10 arcsec of the serial register of the amplifier with the lowest readnoise (Amp B). For non-trivial scenarios (e.g. extended, resolved sources), users should estimate the background level of the observations with the Exposure Time Calculator [3] (ETC).

If the background is too low and it is impossible to increase the exposure time any more, then post-flashing might serve as a viable option for raising the background of the observation. The implementation of post-flashing in the APT assumes a single value of 14 electrons per second, corresponding to partitions A4, B1, C3, D2 in Figure 5, to compute the flash duration required for the specified post-flash level. This means that if the target falls outside of these four partitions, then the actual background at the location of the target will be overestimated by a factor of

$$\beta = \frac{14e^{-}/s}{\overline{p}_{SCI}}, \tag{6}$$

where $\overline{p}_{SCI}$ is the value from Table 2 for the partition containing your target.

The overestimation is highest where CTE effects are lowest and so the consequences are small as the flash signal is added to improve the CTE. However, for more precise calculations of the local background near your target, Table 2 may be used to compute the β scaling value required to account for the non-uniform illumination pattern. For example, if the desired post-flash signal is 20 electrons and the target of interest is located in partition D4, then the requested number of electrons in APT should be $20\beta = 20(1.35) = 27.0$ electrons. In general, if a post-flash signal of N electrons is required to increase the overall background to more than 20 electrons and the target does not fall in partition A4, B1, C3, or D2, then the requested number of electrons in APT should be Nβ.

6 Conclusion

The new method for generating the post-flash reference file excels at separating dark current and flat-field artifacts. This allows us to finally remove effects from transient hot pixels seen in previous post-flash reference files, which in turn allows for a much more accurate removal of post-flash signal. We break down the full-frame post-flash image into 16 equal sized partitions and find the same non-uniform illumination pattern with a maximum variation of ∼51% as found in previous studies (Cox, 2006 and Ogaz et al., 2014). Using these 16 partitions, we present a new technique to accurately estimate post-flash contributions at locations in the periphery of the illumination pattern. We present the initial discovery of an embedded sinusoidal pattern in the optical power output of the LED with a peak-to-peak variation of ∼4%. The period is roughly one year and we postulate that the modulation arises from changes in the ambient temperature around the LED, but more data is required to fully confirm this hypothesis. Moving forward, the ACS Team will continue to monitor this pattern with plans to eventually implement a time-dependent term encapsulating this effect in the FLASHCORR step of CALACS.

[3] http://etc.stsci.edu/etc/input/acs/imaging/

7 Acknowledgments

The author would like to thank the following ACS Team members for their valuable feedback and suggestions: Nimish Hathi, Ralph Bohlin, Jenna Ryon, Marco Chiaberge, Samantha Hoffman, Roberto Avila, and Andrea Bellini. The author would like to thank Steve Arslanian[4] for providing the ACS/WFC schematic, as well as, JWXWINDT dataset used as proxy for the temperature of the OD-800W LED. The author would like to thank Steve Franka[5], Matthew Lallo[6], and George Hartig[6] for helpful discussions about some potential sources that could be driving the modulation.

This work made use of python packages `astropy` (The Astropy Collaboration et al., 2018), `scipy` (Jones et al., 2001–), and `matplotlib` (Hunter, 2007).

References

Cox, C. (2006). *ACS Post-Flash Measurements*. ACS ISR 2006-07. Space Telescope Science Institute.

Hunter, J. D. (2007). "Matplotlib: A 2D graphics environment". In: *Computing In Science & Engineering* 9.3, pp. 90–95. DOI: 10.1109/MCSE.2007.55. URL: https://matplotlib.org/devdocs/index.html.

Johnston, A.H. (2000). "Proton Displacement Damage in Light-Emitting and Laser Diodes". In:

Jones, Eric, Travis Oliphant, Pearu Peterson, et al. (2001–). *SciPy: Open source scientific tools for Python*. URL: http://www.scipy.org/.

Lucas, R.A. et al. (2016). *ACS Data Handbook*. Vol. 8.0. Space Telescope Science Institute.

Ogaz, S., J. Anderson, and D. Golimowski (2015). *Post-Flash Calibration Darks for the Advanced Camera for Surveys Wide Field Channel (ACS/WFC)*. ACS ISR 2015-03. Space Telescope Science Institute.

Ogaz, S., M. Chiaberge, and N.A. Grogin (2014). *Post-Flash Capabilities fo the Advanced Camera for Surveys Wide Field Channel*. ACS ISR 2014-01. Space Telescope Science Institute.

OptoDiode (2017). *OD800W Data Sheet*. URL: http://optodiode.com/pdf/OD-800W.pdf (visited on 2017).

Riess, A. (2002). *A First Look at Cosmic Rays on ACS*. ACS ISR 2002-07. Space Telescope Science Institute.

Sokol, J., J. Anderson, and L.J. Smith (2012). *Assessing ACS/WFC Sky Backgrounds*. ACS ISR 2012-04. Space Telescope Science Institute.

The Astropy Collaboration et al. (2018). "The Astropy Project: Building an inclusive, open-science project and status of the v2.0 core package". In: *ArXiv e-prints*. arXiv: 1801.02634 [astro-ph.IM].

[4]Goddard Space Flight Center
[5]Ball Aerospace
[6]Space Telescope Science Institute

Appendix A Computation of the Cosmic Ray Flux

To enumerate over the number of cosmic rays in a frame, we leverage information generated by the cosmic ray rejection step of `CALACS`, `ACSREJ`. When combining a stack of images to reject cosmic rays, the `ACSREJ` task updates the data quality (DQ) extensions of each input image with a value of 8192 at the locations of all pixels determined to be affected by cosmic rays. The DQ extensions contain all of the information about the quality of a given pixel at (x,y) in the science extensions (SCI); for example, a hot pixel has a value of 16, a warm pixel has a value 64, and a hot pixel that was hit by a cosmic ray has a value of 8208[7]. For this analysis, the goal is to partition the set all of the pixels affected by cosmic rays into distinct subset of pixels affected by the same cosmic ray and we achieve the desired result by applying the theory of connected-component labeling to the DQ extension.

The DQ flags are additive and so we must perform a bitwise AND comparison with 8192 to find all pixels with values of $8192 + 2^n$, where n is some positive integer (4 in the case of a hot pixel). All pixels that evaluate to True are set to 8192, while all pixels that evaluate to False are set to 0 resulting in a binary image where pixels have values of either 8192 or 0. The connected-component labeling algorithm implemented in the python package `scipy.ndimage` is applied to the binary image with the condition that all pixels with a value of 0 be ignored. The 8-connectitvity matrix (Eq. 7) is used to determine if groups of pixels with values of 8192 are attached. This matrix was selected because it encapsulates all possible connections between adjacent pixels.

$$\begin{bmatrix} 1 & 1 & 1 \\ 1 & 1 & 1 \\ 1 & 1 & 1 \end{bmatrix} \tag{7}$$

Cosmic rays that are comprised of less than 3 connected-pixels are rejected as a visual inspection reveals that most of these are false positives triggered by transient hot pixels. The final result is a label with the same dimensions as the input image containing unique integer values for all of the cosmic rays identified and an example may be seen in Figure 15. This label may be used to compute the size of a cosmic ray in attached pixels, the total number of electrons deposited by a cosmic ray, and the incident cosmic ray flux in cosmic rays per second per cm^2.

[7] The complete list is available at http://www.stsci.edu/hst/acs/analysis/reference_files/data_quality_flags.html

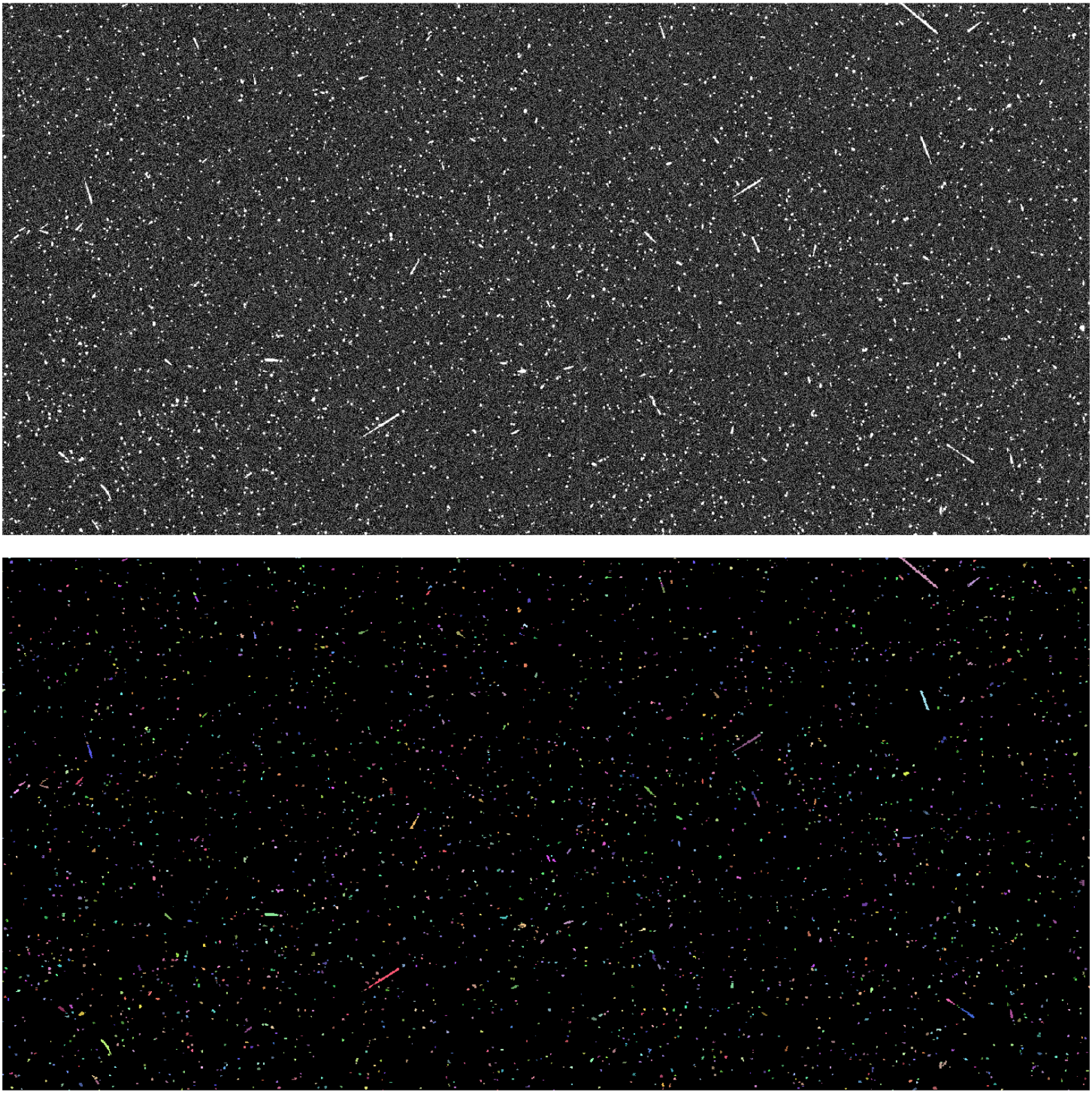

Figure 15: Cosmic ray label

A detailed explanation of this approach will be presented in its own Instrument Science Report (Miles, in prep). For the purposes of this study we simply report a quick test where we compute the total electron deposition for each individual cosmic ray and compare our distribution of values with results detailed in ACS ISR 2002-07 (Riess, 2002). From Figure 16 we see that the distributions are nearly identical with a clear minimum at around 500 electrons and a median cosmic ray total deposition of ∼1000 electrons.

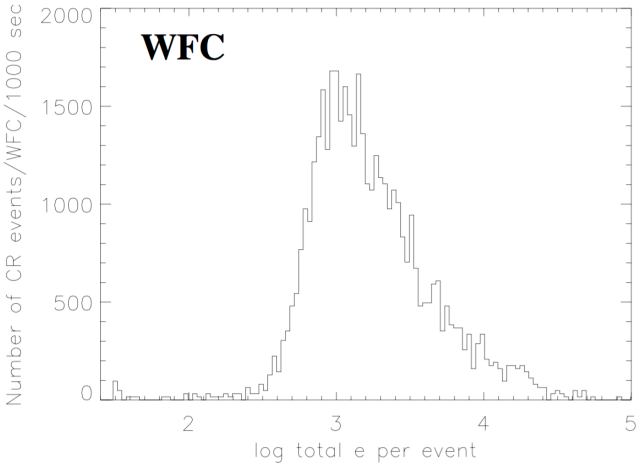

(a) Figure 6 from ACS ISR 2002-07 (Riess, 2002).

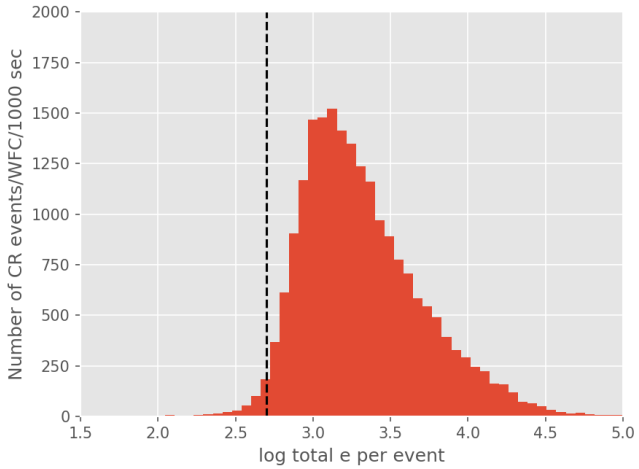

(b) Total electron deposition derived by applying the results from connected-component labeling. The dashed vertical line corresponds to $log(500e)$.

Figure 16

With the capability to individually label each cosmic ray, deriving the incident cosmic ray rate is just a matter of counting up the number of labels and dividing by the total integration time. We define the total integration time to be the sum of the EXPTIME keyword and 45 seconds, where the value of 45 seconds is added to account for cosmic rays hitting the detector during the readout process which takes ∼ 90 seconds to complete. The incident cosmic ray rate is computed for approximately 9,000 bias-corrected dark frames taken between 2002 and 2018 which spans two solar maxima and one solar minimum.

It is well-known that the galactic cosmic ray intensity is modulated by the solar cycle with the minimum intensity occurring at the maximum of the solar cycle and the maximum intensity occurring at the minimum of the solar cycle. Solar cycle 23 attained a maximum in November of 2001, while solar cycle 24 started at the next minimum in December of 2008 and subsequently reached its maximum in April of 2014. From Figure 17, we see the modulation is at the level of 20% peak-to-peak and that the minima of the incident cosmic ray rate occur at roughly the solar cycle maxima and the maximum occurs during the only solar cycle minimum from 2002 to 2018. The average incident cosmic ray rate, as observed by the ACS/WFC detector, is 44 $\frac{events}{s}$ and so using the geometric area we calculate the flux to be $44\frac{events}{s} * \frac{1}{37.786cm^2} = 1.164\frac{events}{s*cm^2} \approx 1.2\frac{events}{s*cm^2}$.

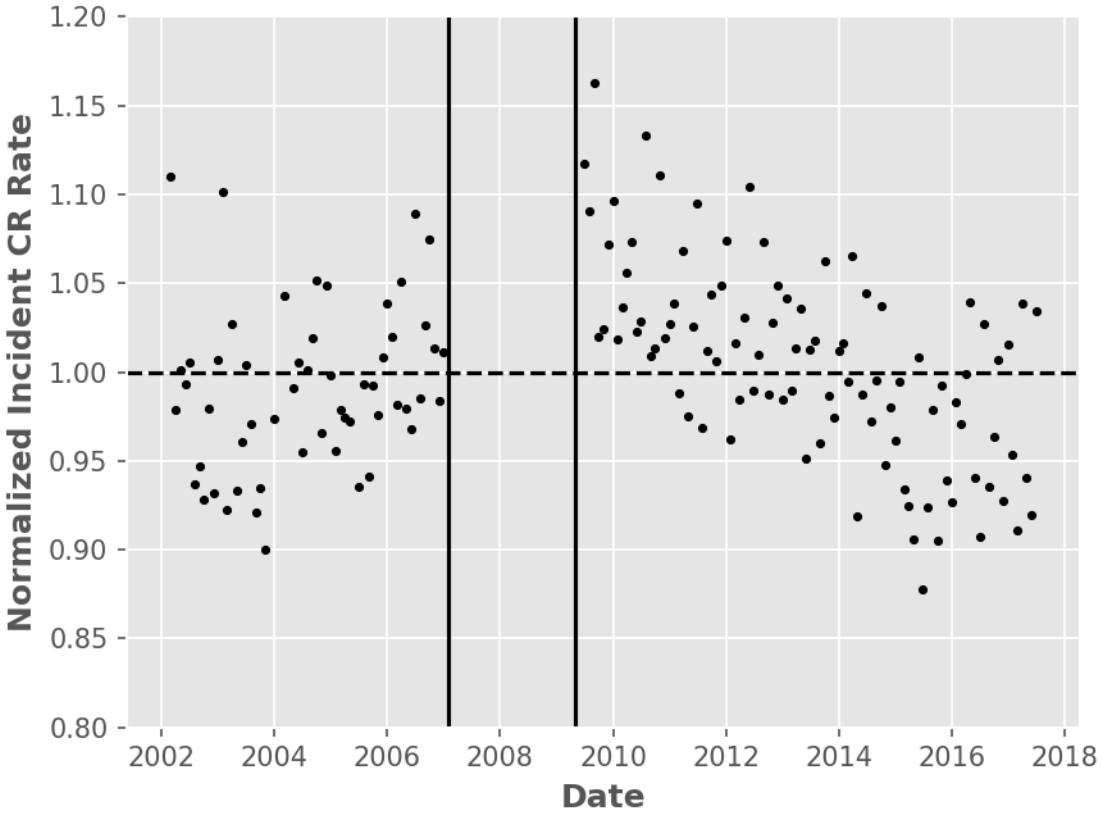

Figure 17: Mean normalized cosmic ray rate derived from 1000 second dark frames taken since 2002. A one month rolling average has been applied to smooth the data.